Influence of Ce$_2$O$_3$ and CeO$_2$ promoters on Pd/MgO catalysts in the dry-reforming of methane

Faris A. J. Al-Doghachi,[ab] Umer Rashid,[c] Zulkarnain Zainal,[ab] Mohd Izham Saiman[ab] and Yun Hin Taufiq Yap*[ab]

In this study, the conversion of methane and CO$_2$ to synthesis gas using dry reforming over Pd/MgO catalysts using different concentrations of Ce^{3+} and Ce^{4+} was investigated. Moreover, the factors that contribute to the deposition of carbon during the co-precipitation method were examined. The catalysts used in this study were prepared using K$_2$CO$_3$ as the precipitant. The characterization of the catalysts was performed using state-of-the-art techniques such as XRD, XPS, FT-IR, TPR-H$_2$, BET, TEM, FE-SEM, and TGA. It was found that with the addition of Ce promoter, the Pd/Mg$_{0.85}$Ce$_{015}$O catalyst exhibited a high level of activity (CH$_4$: 54%, and CO$_2$: 74%) with excellent stability. The results of this analysis also revealed the outstanding anti-coking activity of the reduced catalyst with low Pd metal. In addition, we studied the catalytic performance and stability of the produced catalysts.

1. Introduction

The production of biogas (CO$_2$ and CH$_4$) from the anaerobic digestion of biomass (fermented wastes) has been directly exploited as a fuel for small-to-medium-scale combined heat production as well as power production. It has also been used as a renewable carbon source in the production of synthesis gas (syngas) (CO and H$_2$) for industrial feedstock through an economically and environmentally friendly reaction.[1] The alternative method to this energy intensive process is to use steam reforming of methane, which is a well-established production route, as shown in eqn (1),[2] or the use of carbon dioxide as an oxidant, commonly known as the 'dry reforming process', as shown in eqn (2).

$$CH_4 + H_2O \rightarrow 3H_2 + CO, \; \Delta H_{298 \; K} = +225.4 \text{ kJ mol}^{-1} \quad (1)$$

$$CH_4 + CO_2 \rightarrow 2H_2 + 2CO, \; \Delta H_{298 \; K} = +247.3 \text{ kJ mol}^{-1} \quad (2)$$
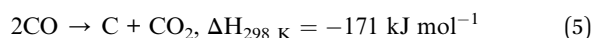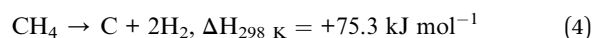
Syngas is a vital feedstock, which can be effectively converted to ultra clean fuels, such as methanol, gasoil, gasoline, and dimethyl ether (DME), through the use of the Fischer–Tropsch synthesis.[3] The equilibrium of the reaction during the production of syngas from CH$_4$ and CO$_2$ (eqn (2)) is affected by the

simultaneous reverse water-gas shift (RWGS) reaction (eqn (3)). The resulting effect is a low H$_2$/CO ratio.

$$CO_2 + H_2 \rightarrow H_2O + CO, \; \Delta H_{298 \; K} = +41.2 \text{ kJ mol}^{-1} \quad (3)$$
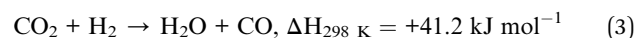
Moreover, the dry reforming reaction is associated with other side reactions such as the decomposition of methane (eqn (4)), as well as the disproportionation reaction (Boudouard reaction) (eqn (5)).

$$CH_4 \rightarrow C + 2H_2, \; \Delta H_{298 \; K} = +75.3 \text{ kJ mol}^{-1} \quad (4)$$

$$2CO \rightarrow C + CO_2, \; \Delta H_{298 \; K} = -171 \text{ kJ mol}^{-1} \quad (5)$$

Zhang *et al.*[4] reported that CH$_4$ decomposition (eqn (4)) and CO disproportionation (eqn (5)) show a direct relation to carbon deposition on the catalyst. When the temperature of the reaction increases from 550 °C to 650 °C, a greater tendency for the deposition of carbon rather than the DRM is observed. Thus, the choice of catalyst plays a crucial role in the prevention of carbon formation and also improves the DRM reaction. Furthermore, the deposition of carbon can be reduced or even eliminated through the support of metal in a metal oxide (MO) with strong basicity.[5] This occurs because an increase in the basicity of the support causes the catalyst to chemisorb CO$_2$ in the CO$_2$ reforming of methane. Consequently, these species react with C to form CO (eqn (6)).

$$CO_{2(g)} + C_{(s)} \rightarrow 2CO_{(g)} \quad (6)$$
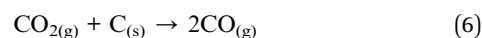
It is important to consider two remarkably significant factors in the design of anti-carbon deposition catalysts. The first factor is that the deposition of carbon can only take place when the

ᵃCatalysis Science and Technology Research Centre, Faculty of Science, Universiti Putra Malaysia, UPM, Serdang, 43400, Selangor, Malaysia. E-mail: taufiq@upm. edu.my; Fax: +60-3-89466758; Tel: +60-3-89466809

ᵇDepartment of Chemistry, Faculty of Science, Universiti Putra Malaysia, UPM, 43400 Serdang, Selangor, Malaysia

ᶜInstitute of Advanced Technology, Universiti Putra Malaysia, UPM 43400 Serdang, Selangor, Malaysia

metal cluster is greater than the critical size. The other factor is that carbon deposition is favored by an acidic support. Thus, it is obvious that the size of the metal cluster must be smaller than the critical size, which is required for coke formation to prevent the deposition of carbon; moreover, the acidity of the support must also be reduced. Thus, the best way to reduce the acidity is to select basic metal oxides, such as alkaline earth metal oxides, that can function as effective supports.[6] The selection of MgO as a support lies in its properties that allow for the prevention of acidity and control of the size of Ni particles through the use of small amounts of NiO. This is one way to prevent the deposition and sintering of the carbon. The other two factors that have encouraged researchers to select MgO as a support include its high thermal stability with its high melting point of 2850 °C, and its rather low cost of production.[7]

It is evident that the performance of a supported catalyst can be easily improved by the selection of proper promoting materials. It has also been found that supported transition metals, particularly Ni, Ru, Rh, Pd, and Ir, have considerable effects on reforming reactions. It has been reported that noble metals are more active but have less sensitivity to coking. However, supported nickel is the preferred choice; it is used more frequently in industrial reforming processes because it is readily available and its cost is low.[8,9] Seshan *et al.*[10] performed evaluations of several catalytic formulations with Ni or Pt supported on ZrO_2. The findings revealed Pt/ZrO_2 to be a very stable catalyst throughout the reaction, in comparison to a Ni-based catalyst.[11]

The use of alkaline promoters, such as CaO, can efficiently prevent sintering. Dias and Assaf[12] discovered that when calcination occurs, sintering can cause deactivation during the preparation of catalysts. Recently, Juan-Juan *et al.*[13] examined the benefits of the addition of potassium to the catalyst. It was found that the pre-treating of nickel species with hydrogen could further reduce the nickel species. Likewise, Luna and Iriarte[14] discovered that the addition of potassium could prevent the accumulation of carbon on the surface of the catalyst. Numerous studies[15,16] have reported that CeO_2 can reversibly store and release a large amount of oxygen in response to gas phase concentration. This feature is referred to as oxygen storage capability (OSC). Although there have been extensive studies on MgO, ZrO_2 and Al_2O_3, as catalyst promoters, there are few investigations into the use of Ce^{3+} and Ce^{4+} as promoters of Pd/MgO for DRM.[17]

Ceria is frequently used as a preferred promoter because of its high oxygen storage/transport capacity. In fact, ceria plays a significant role as a promoter in DRM reactions, due to its ability to supply oxygen from its lattice and its ability to replace oxygen with the support through the dissociation of CO_2 on its surface.[18] The adsorption and activation of CO_2 occur on the surface sites of Ce^{3+} while CO is formed and Ce^{3+} is simultaneously oxidized to Ce^{4+}. Because ceria can chemisorb large amounts of H_2 and CO, its intake depends on the thermal treatment conditions and its own surface/bulk properties.[19] In addition to the effects of ceria as a promoter on the dissociative adsorption of CO_2, it is capable of enhancing the stabilization and dispersion of small metal particles. This can lead to significant changes to the surface features of both the metal and

the oxide.[20] Therefore, it is postulated that the high thermal stability of the dispersed metal, as well as the formation of Ce–M alloys in a reductive atmosphere, is due to the strong metal-support interaction (SMSI) effect. Because SMSI reduces catalytic activity, bulk Ce_2O_3 is not a proper support for nickel. Recently, many research studies employed DRM to develop improved Ce with ternary and binary supports.[21,22]

Thus, the present study aims to investigate the effects of Ce^{3+} and Ce^{4+} as promoters on MgO, which acts as a carrier, and the effects of doping Pd metal on the surface of the support were also investigated. A comparison of the activity and stability of the promoter catalysts and non-promoter Pd/MgO catalyst was carried out to better understand the effects of the promoter on the performance of the catalyst during the DRM reaction. The catalysts were also characterized by chemical analysis, nitrogen adsorption desorption measurements, XRD, XPS, FT-IR, HRTEM, BET, TGA and FE-SEM-EDS.

2. Experimental

2.1. Preparation of the catalysts

The $Mg_{1-x}Ce_x^{3+}O$ catalysts (x = 0.00, 0.03, 0.07, 0.15) were prepared using the co-precipitation method.[23] Moreover, the support MgO and promoter Ce_2O_3 were prepared using 0.1 M aqueous solution of $Ce(NO_3)_3 \cdot 6H_2O$ (Merck; >99.0%) and $Mg(NO_3)_2 \cdot 6H_2O$ (Merck; >99.0%) and 1 M K_2CO_3 (Merck; >99.7%), which were used as precipitants. The sample was rinsed with hot water after the filtration of the precipitant. Then, the sample was dried at 120 °C for 12 h. Subsequently, the sample was pre-calcined in air at 500 °C for 5 h to remove CO_2 from the precipitant. The sample was then pressed into disks at 600 kg m^{-2}, followed by calcination at 1150 °C for 20 h to enhance the mechanical properties and ensure good interaction between the MgO support and the promoter Ce_2O_3.

Table 1 shows the preparation of the catalyst. Initially, 1% Pd was impregnated using $Pd(C_5H_7O_2)_2$ (Aldrich; >99%), which was dissolved in dichloromethane. After impregnation in air, the catalysts were dried for 12 h at a temperature of 120 °C. The dried catalysts were sieved and then ground into particles of 80–150 or 150–250 μm in diameter. The same process was used for the $Pd/Mg_{1-x}Ce_x^{4+}O$ (x = 0.03, 0.07, 0.15) catalysts. The only change was that $Ce(NO_3)_3 \cdot 6H_2O$ salt was replaced with $(NH_4)_2Ce(NO_3)_6 \cdot 6H_2O$ salt.

2.2. Catalyst characterization

The thermogravimetric analysis (TGA) was accomplished on a Mettler Toledo TG-DTA Apparatus (Pt crucibles, Pt/Pt–Rh thermocouple) with a purge gas (nitrogen) flow rate of 30 ml min^{-1} and a heating rate of 10 °C min^{-1} from 50 to 1000 °C.

The XRD analysis was performed using a Shimadzu diffractometer (XRD 6000). The diffractometer used Cu-Kα radiation at ambient temperature to obtain diffraction patterns from crystalline powder samples. Cu-Kα radiation was obtained using a Philips glass diffraction X-ray tube broad focus 2.7 kW type. The size D crystallites of the samples were measured using the Debye–Scherrer relationship,[24] where D is the crystalline size,

Table 1 Preparation of catalysts with prepared 0.1 M solutions of the mixed promoter and support followed by determining the total weight of MgO with promoter after precipitation with 1 M K_2CO_3 and calcination at 1150 °C

Catalyst	Support (MgO) using $Mg(NO_3)_2 \cdot 6H_2O$ (g)	Promoter (Ce_2O_3 or CeO_2) using $Ce(NO_3)_3 \cdot 6H_2O$ or $(NH_4)_2Ce(NO_3)_6 \cdot 6H_2O$ (g)	Total weight of MgO and (Ce_2O_3 or CeO_2) (g)	Impregnation of the main catalyst (1% Pd) with $Pd(acac)_2$ (g)
Pd/MgO	25.00	0.00	1	0.03
$Pd/Mg_{0.97}Ce_{0.03}{}^{3+}O$	24.9	1.3	1	0.03
$Pd/Mg_{0.93}Ce_{0.07}{}^{3+}O$	23.8	3.0	1	0.03
$Pd/Mg_{0.85}Ce_{0.15}{}^{3+}O$	21.8	6.5	1	0.03
$Pd/Mg_{0.97}Ce_{0.03}{}^{4+}O$	24.8	1.6	1	0.03
$Pd/Mg_{0.93}Ce_{0.07}{}^{4+}O$	23.8	3.8	1	0.03
$Pd/Mg_{0.85}Ce_{0.15}{}^{4+}O$	21.8	8.2	1	0.03

λ is the incident X-ray wavelength, β is the full width at half-maximum (FWHM), and θ is the diffraction angle.

Fourier transform infrared (FT-IR) analysis was conducted on a PerkinElmer spectrometer model 100 series (sample preparation UATR).

The total catalyst surface area was obtained with nitrogen gas adsorption at −196 °C using the Brunauer–Emmett–Teller (BET) method. The analysis was carried out using a Thermo Fisher Scientific S.P.A. (model: Surfer Analyzer) nitrogen adsorption–desorption analyzer.

Transmission electron microscopy (TEM) (Hitachi H7100 TEM with accelerating voltage of 10 MV) was used to determine the crystal shapes and the homogeneity of the catalysts.

The sample morphology was studied by field emission scanning electron microscopy (FE-SEM) (JEOL-FE-SEM model JSM 7600F) at very high magnification using field emission current. The sample was coated with gold to ensure enhanced visibility of the surface and to prevent the electrical charging of the sample during analysis.

The active sites of the catalysts were evaluated by temperature-programmed reduction (H_2-TPR) (Thermo Finnegan TPDRO 1100) equipped with a thermal conductivity detector. About 0.05 g of catalyst was placed in a reactor and treated at 150 °C for 30 min in N_2 (20 ml min^{-1}). The analysis of hydrogen (5.51% in argon) was conducted at 50 °C and 950 °C under an argon flow (10 °C min^{-1}, 25 ml min^{-1}) and was detected by the thermal conductivity detector.

XPS analysis was performed using a Kratos Axis Ultra DLD system equipped with monochromatic Al Kα (1486.6 eV), dual X-ray sources (Al and Mg), an argon etching system for sample cleaning and depth profiling, parallel imaging XPS, AES, and ISS, and Vision software to control the system. The base pressure of the analyzer chamber was 1×10^{-10} Torr. The excitation source, an X-ray gun, was operated at a combination of 20 mA of emission current and 15 kV voltage. The hemispherical analyzer was run using the fixed analyzer transmission (FAT) mode for both wide and narrow scanning. The values were set at 100 eV and 40 eV of pass energy, respectively. The region of interest for the narrow scan corresponded to the C1s, Mg2p, Ce3d, Pd3d, and O1s photoelectron signals. The carbon charging correction refers to the binding energy of adventitious carbon at a binding energy of 285 eV. This highly sophisticated equipment is considered to represent a non-destructive analysis technique because it uses soft X-ray production to induce photoelectron emission from the sample surface. Therefore, the equipment can provide information about surface layers or thin film structures (about the top 10–100 Å of the sample).

2.3. Catalytic evaluation

The catalytic evaluation of the dry reforming of methane was carried out using a fixed bed stainless steel micro-reactor (i.d. Ø = 6 mm, h = 34 cm). The reactor was attached to a mass flow gas controller (Sierra Instruments) and an online gas chromatograph (GC) (Agilent 6890N; G 1540N) equipped with Varian capillary columns (HP-PLOT/Q and HP-MOLSIV). Before the reaction, approximately 0.02 g catalyst was reduced by a flow of 5% H_2/Ar (30 ml min^{-1}) at 700 °C with a holding period of 3 h. The reforming reaction was performed by flowing the feed, which is a gas mixture composed of CH_4/CO_2 at (2/1) and (1/1) molar ratios, at a rate of 30 ml min^{-1}. The reforming was studied from 700 to 900 °C at 1 atm; holding was then carried out for 10 h (1 atm, GHSV = 15 000 ml h^{-1} g^{-1} cat).

The aim of the reduction step was to reduce the (Pd^{2+}) phase of the palladium catalyst to Pd metal (Pd^0) phase at the active site of the catalysts. The tested catalyst was set vertically in the middle of the reactor and fixed in place using plugs of quartz wool. To control and measure the reaction temperature, a thermocouple was placed in the catalyst chamber. The calculations of methane and carbon dioxide conversions and H_2 and CO selectivity, as well as the synthesis gas (H_2/CO) ratio, were defined with the following equations (eqn (7)–(11)).

$$CH_4 \text{ conversion}\% = \frac{CH_{4in} - CH_{4out}}{CH_{4in}} \times 100 \tag{7}$$

$$CO_2 \text{ conversion}\% = \frac{Co_{2in} - CO_{2out}}{Co_{2in}} \times 100 \tag{8}$$

$$H_2 \text{ selectivity}\% = \frac{H_2}{2[CH_{4in} - CH_{4out}]} \times 100 \tag{9}$$

$$CO \text{ selectivity}\% = \frac{CO}{[CH_{4in} - CH_{4out}] + [CO_{2in} - CO_{2out}]} \times 100 \tag{10}$$
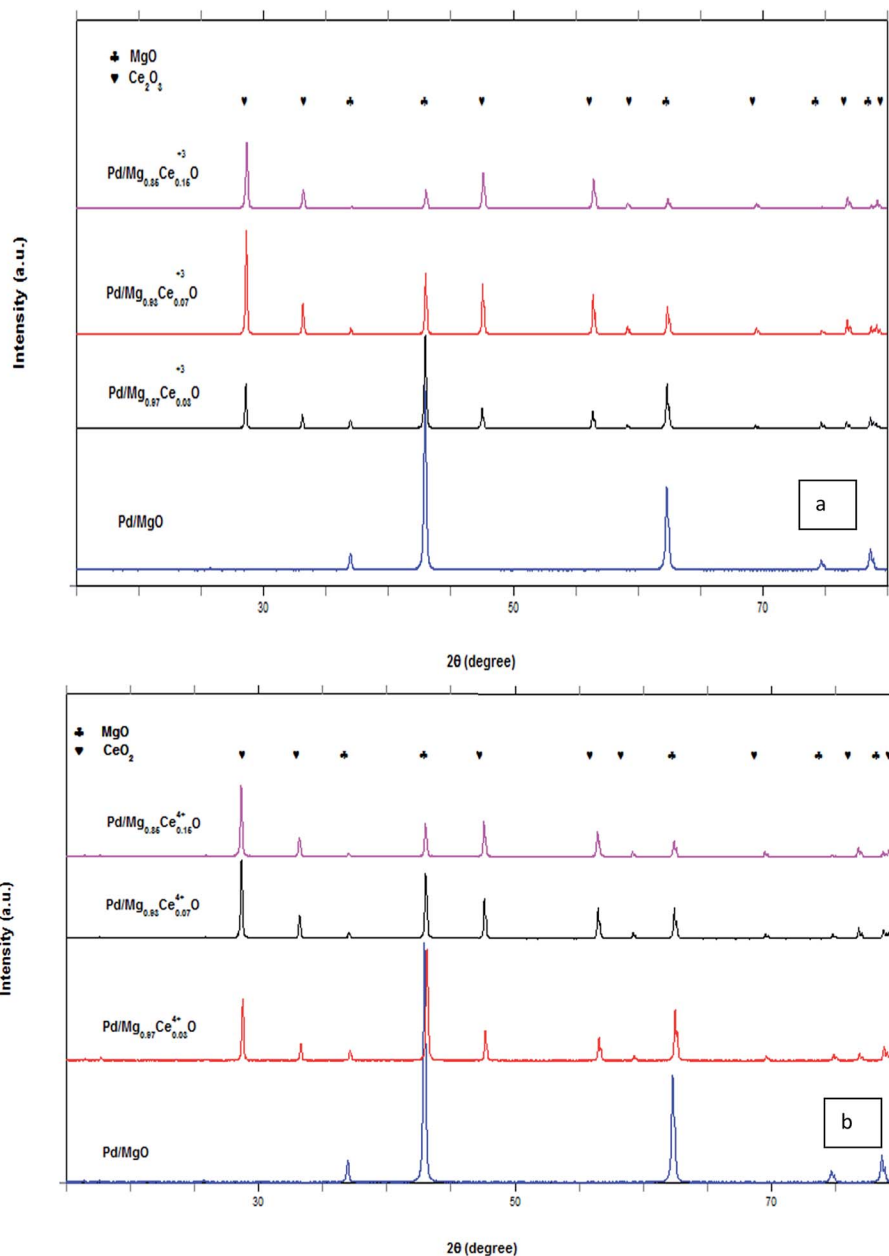
Fig. 1 XRD patterns of the catalysts with (a) Ce^{3+} and (b) Ce^{4+} promoter.

Table 2 The main textural properties of the fresh catalysts

Sample name	Specific surface area[a] ($m^2\ g^{-1}$)	Pore volume ($cm^3\ g^{-1}$)	Pore radius (Å)	Average crystal size[b] (nm)
Pd/MgO	15.7	0.2122	11.4	47.3
Pd/Mg$_{0.97}$Ce$_{0.03}$$^{3+}$O	6.3	0.0946	23.6	59.2
Pd/Mg$_{0.93}$Ce$_{0.07}$$^{3+}$O	7.5	0.1055	24.3	60.9
Pd/Mg$_{0.85}$Ce$_{0.15}$$^{3+}$O	16.6	0.123	90.1	62.3
Pd/Mg$_{0.97}$Ce$_{0.03}$$^{4+}$O	8.1	0.116	23.3	53.6
Pd/Mg$_{0.93}$Ce$_{0.07}$$^{4+}$O	9.3	0.134	25.6	57.2
Pd/Mg$_{0.85}$Ce$_{0.15}$$^{4+}$O	9.8	0.1433	30.9	58.5

[a] Specific surface area calculated by BET method. [b] Determined by the Debye–Scherrer equation of the Mg (200) plane of XRD.

$$\frac{H_2}{CO} \text{ratio} = \frac{H_2 \text{ selectivity\%}}{CO \text{ selectivity\%}} \quad (11)$$

surface of the catalyst with a few nanometer layers of 3–12 nm by XPS revealed the emittance of photoelectron signals from C1s, Mg2p, O1s, Pd3d, and Ce3d and distinguished between

3. Results and discussion

3.1. Characterization of catalysts

3.1.1 XRD patterns. Fig. 1a and b illustrate the XRD patterns of the reduced catalysts, inclusive of magnesium and cerium. Fig. 1 also shows the diffraction peaks that occur at $2\theta = 37.0°$, $62.3°$, $74.7°$ and $79.1°$ due to the cubic form of magnesia (JCPDS file no.: 00-002-1207). Moreover, the diffraction peaks at $2\theta = 28.7°$, $33.3°$, $47.8°$, $56.8°$, $59.6°$, $69.6°$, $76.8°$ and $79.3°$ appeared as a result of the cubic form of ceria (JCPDS file no.: 00-001-0800). However, no diffraction peaks were observed for 1% palladium in all the patterns. This may be due to the very low concentration of palladium. This observation was in agreement with the results reported by Grange.[25] The diffraction peak of the Mg plane in the XRD patterns, which was determined by the use of the Debye–Scherrer equation (Table 2), was used to check the average crystalline size. It was found that the crystalline size was in direct proportion with the amount of ceria in the catalysts. This may be due to the effects of the remaining palladium, which rests on the surface of the samples and prevents the growth of magnesia crystallites. The measurements for the sizes of the crystals were recorded as 47.3, 59.2, 60.9, and 62.3 nm for Pd/MgO, Pd/$Mg_{0.97}Ce_{0.03}^{3+}O$, Pd/$Mg_{0.93}Ce_{0.07}^{3+}O$, and Pd/$Mg_{0.85}Ce_{0.15}^{3+}O$, respectively. However, the sizes of the Pd/$Mg_{0.97}Ce_{0.03}^{4+}O$, Pd/$Mg_{0.93}Ce_{0.07}^{4+}O$, and Pd/$Mg_{0.85}Ce_{0.15}^{4+}O$ crystals were recorded as 53.6, 57.2, and 58.5 nm, respectively. The crystal systems for all the samples were recorded in cubic shape due to the cubic shaped particles inside the catalysts;[26] the XRD results were also supported by TEM and FESEM.

3.1.2 FT-IR spectra. Fig. 2a and b shows the FT-IR data of the sample, which was prepared through the impregnation of $Pd(acac)_2$ on $MgO–Ce_2O_3$. The spectra of the unreduced catalysts showed bands in the region of 1800–1000 cm^{-1}, which are characteristic of acetylacetonate ligands. The bands recorded at 1654 and 1548 cm^{-1} in the FT-IR were assigned to the C=O and C=C bonds of acetylacetonate in the main catalyst ($Pd(acac)_2$) complex. Fig. 2a also shows other bands in the spectra, which indicate the presence of acetylacetonate. The bands appeared at 1353, 1262, and 1200 cm^{-1}, and these readings correspond to C–H bonds in CH_3 (bending), C–C (stretching), and C–H (bending), respectively. The band at 936 cm^{-1} corresponds to C–O bond, while the peak at 671 cm^{-1} corresponds to Ce–O, as per reported data.[27] The results for $Pd(acac)_2/Mg_{0.97}Ce_{0.03}^{4+}O$, $Pd(acac)_2/Mg_{0.93}Ce_{0.07}^{4+}O$, and $Pd(acac)_2/Mg_{0.85}Ce_{0.15}^{4+}O$ were similar, as observed in Fig. 2b. It can be concluded that FT-IR was unable to detect the Pd–O bond because it lies in the far FT-IR region. However, all the acetylacetonate peaks disappeared after reduction with hydrogen at a temperature of 700 °C, as shown in Fig. 2c.[28,29]

3.1.3 XPS analysis. XPS analysis was used to obtain information about the surface composition of the unreduced $Pd(acac)_2/Mg_{0.85}Ce_{0.15}^{3+}O$ catalyst. An examination of the
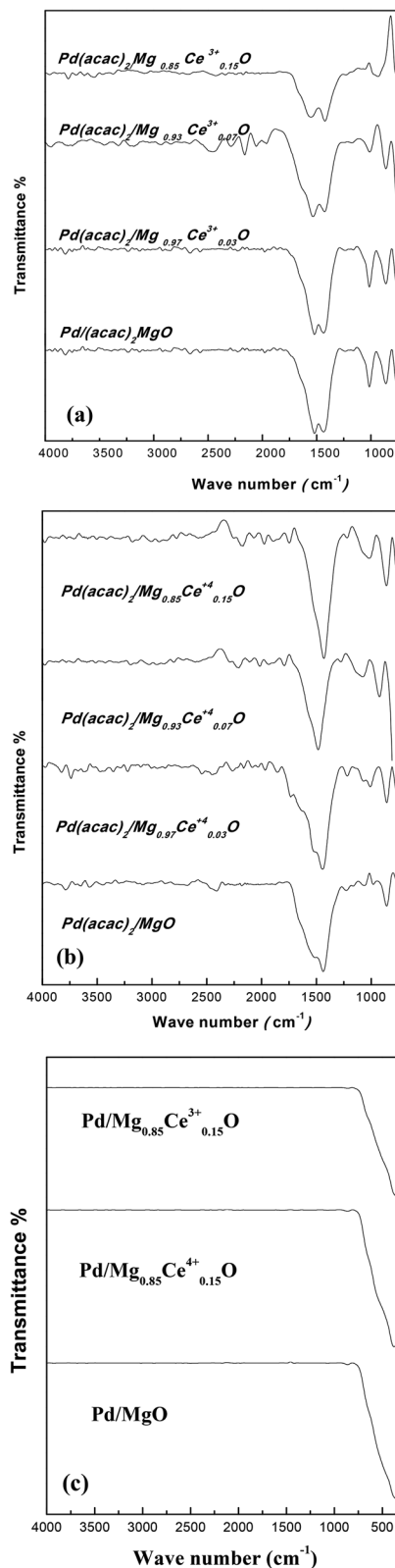
Fig. 2 FT-IR spectra for the catalysts with (a) Ce^{3+} promoter, (b) Ce^{4+} promoter, and (c) after reduction of the catalysts.
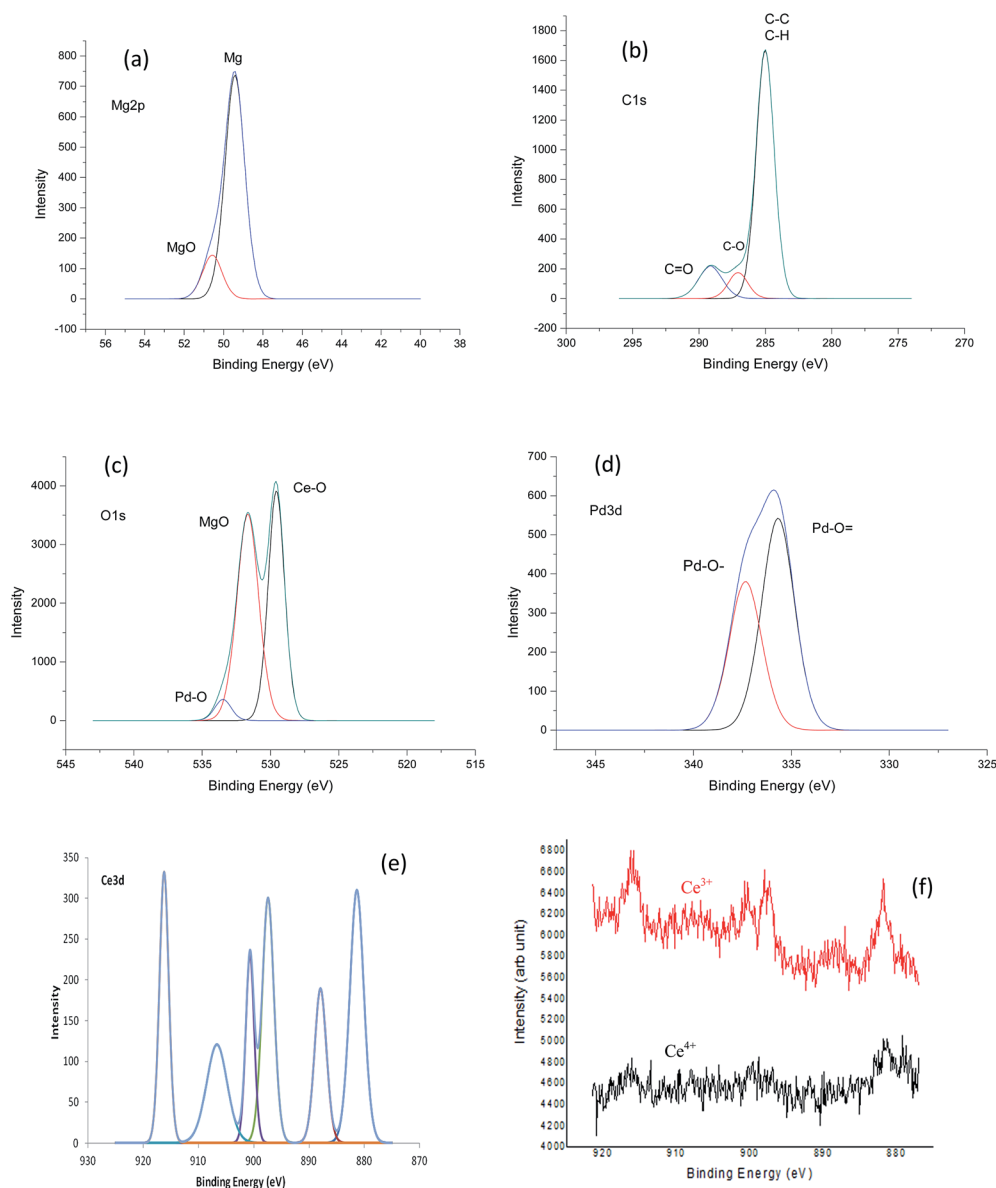
Fig. 3 XPS narrow scans of $Pd(acac)_2/Mg_{0.85}Ce_{0.15}{}^{3+}O$ catalyst. (a) Mg2p, (b) C1s, (c) O1s, (d) Pd3d, (e) Ce3d and (f) distinguishing between Ce^{3+} and Ce^{4+}.

Ce^{3+} and Ce^{4+}, as shown in Fig. 3a–f. Three types of carbon species were observed, as indicated by the deconvolution of a C1s narrow scan; the carbon species were identified to be C–C (or C–H), C–O and C=O. The O1s photoelectron signal was produced by three types of oxygen species, namely, Mg–O, Ce–O, and Pd–O. This was also a significant split in the O1s spectrum. Two peaks were formed from Mg2p (Mg–O and Mg). The peak formed by Ce–O showed the highest photoelectron signal intensity in the high binding energy region compared to the other peaks. Moreover, the narrow scan of Mg2p, Ce2p and Pd3d revealed that the composition of the oxide species of these metals was a mixture of Mg–O, Ce–O and Pd–O, respectively.[30,31]

The XPS spectra showed that the solid solution of $Ce_2O_3/$ MgO recorded the lowest and highest binding energies of 51 and 882 eV for Mg2p and Ce3d, respectively. This caused electron transfer from Ce_2O_3 to MgO, which slowed the reduction rate of Ce_2O_3 during the preparation of the reduced catalyst. This could lead to an increase in the interaction between the two oxides, followed by the segregation of Ce atoms into tiny particles that rest on the surface of the catalyst. Consequently, there was a high dispersion of Ce, which accounted for the high activity of the catalyst. Following the extraction of the substrate, the segregated Ce particles interacted strongly with the remaining Ce on the substrate, resulting in the attenuation of their sintering. Coke formation, which requires large Ce clusters, was prevented by the high dispersion of Ce. The TEM analysis revealed that the Ce_2O_3–MgO solid solution, which was highly effective, consists of crystallite sizes of about 80 nm. The solid solution was unchanged throughout 50 h of reaction at 900 °C.[32]
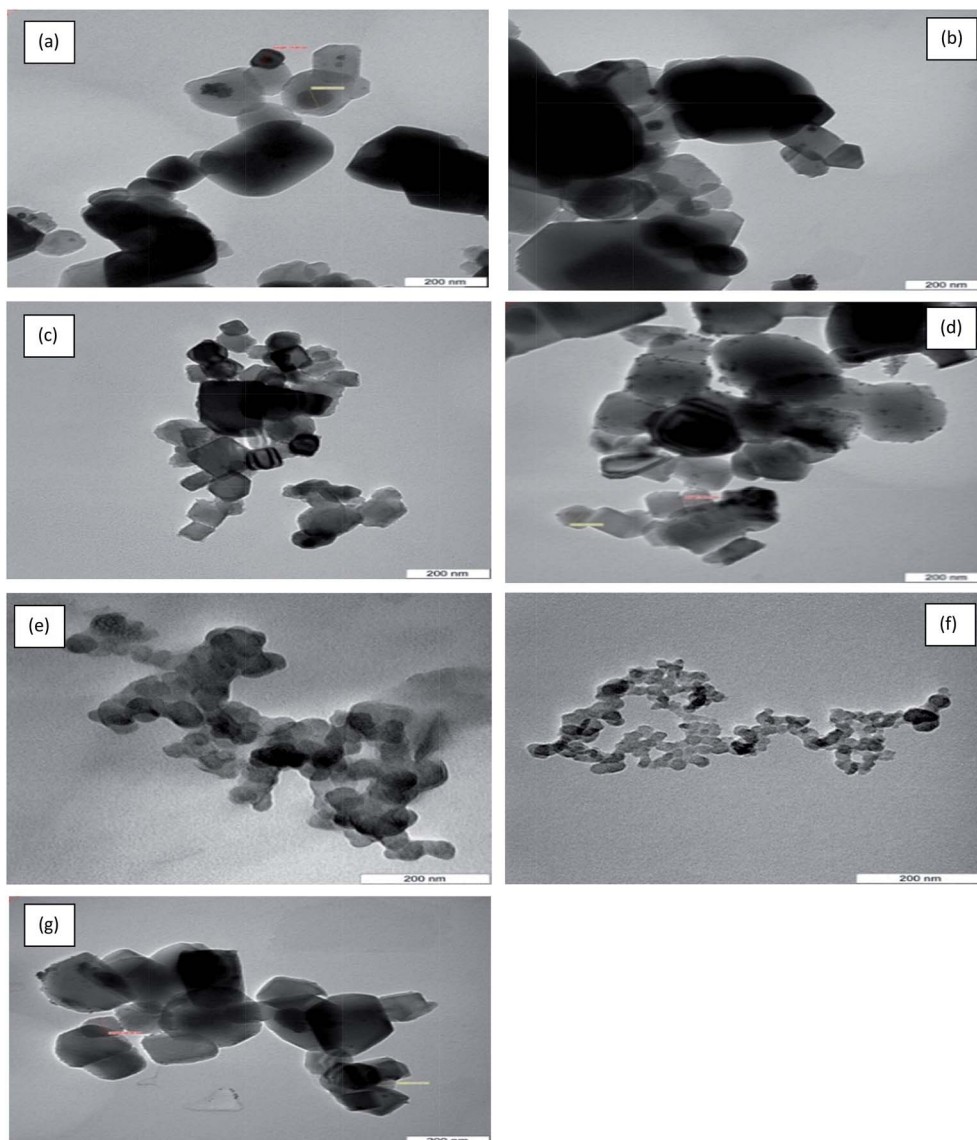
Fig. 4 TEM images of catalysts: (a) Pd/MgO, (b) Pd/Mg$_{0.97}$Ce$_{0.03}$$^{3+}$O, (c) Pd/Mg$_{0.93}Ce_{0.07}$$^{3+}$O, (d) Pd/Mg$_{0.85}Ce_{0.15}$$^{3+}$O, (e) Pd/Mg$_{0.97}Ce_{0.03}$$^{4+}$O, (f) Pd/Mg$_{0.93}Ce_{0.07}$$^{4+}$O and (g) Pd/Mg$_{0.85}Ce_{0.15}$$^{4+}$O.

In this study, XPS was used for the analysis of the Pd/Mg$_{0.85}$Ce$_{0.15}$$^{4+}$O compound. It was noted that there were differences between the Ce3d peaks of Pd/Mg$_{0.85}$Ce$_{0.15}$$^{4+}$O and Pd/Mg$_{0.85}Ce_{0.15}$$^{3+}$O. As shown in Fig. 3f, Ce(III) and Ce(IV) spectra have different multiplet splitting; therefore, Ce(IV) showed a peak at 917 eV, which was absent in the Ce(III) spectrum. The concentration of Ce^{3+} was observed to be high compared to that of Ce^{4+}; thus, Ce^{3+} showed greater activity and stability as well.

3.1.4 TEM and FE-SEM. Fig. 4a–g illustrates the distribution, morphology and size of the synthesized catalysts. The smallest crystals, approximately 50–80 nm, were characterized by TEM through the analysis of the cubic structures and crystal sizes. Fig. 5a–g show the morphology of the catalyst, which was supported by the FE-SEM analysis. It was found that regularly shaped particles support the Pd/Mg$_{0.97}$Ce$_{0.03}$$^{3+}$O, Pd/Mg$_{0.93}Ce_{0.07}$$^{3+}$O, and Pd/Mg$_{0.85}Ce_{0.15}$$^{3+}$O catalysts.[33] Moreover,

the crystalline Pd particles uniformly supported the regularly shaped supports, which results in smaller Pd particles and greater homogeneity in the metal dispersion. Fig. 4a–g illustrate the two-dimensional cubic texture of the catalyst.[34] The pores of the catalyst were uniformly sized at ∼18 nm, which was also consistent with the BET results, as presented in Table 2. Some of the Pd particles were uniformly loaded on the external surface of the Mg$_{0.85}$Ce$_{0.15}$O support, which varies considerably from the crystalline sites inside the porous structure. The difference in the sizes of the Pd particles may be due to the growth of regulated crystals inside the narrowly distributed channels, thus resulting in reduced homogeneity of the Pd particles in comparison to the other catalysts. It was found that the particle size of the supported Pd showed an increase in the following sequence: Pd/Mg$_{0.85}$Ce$_{0.15}$$^{3+}$O < Pd/Mg$_{0.93}Ce_{0.07}$$^{3+}$O <
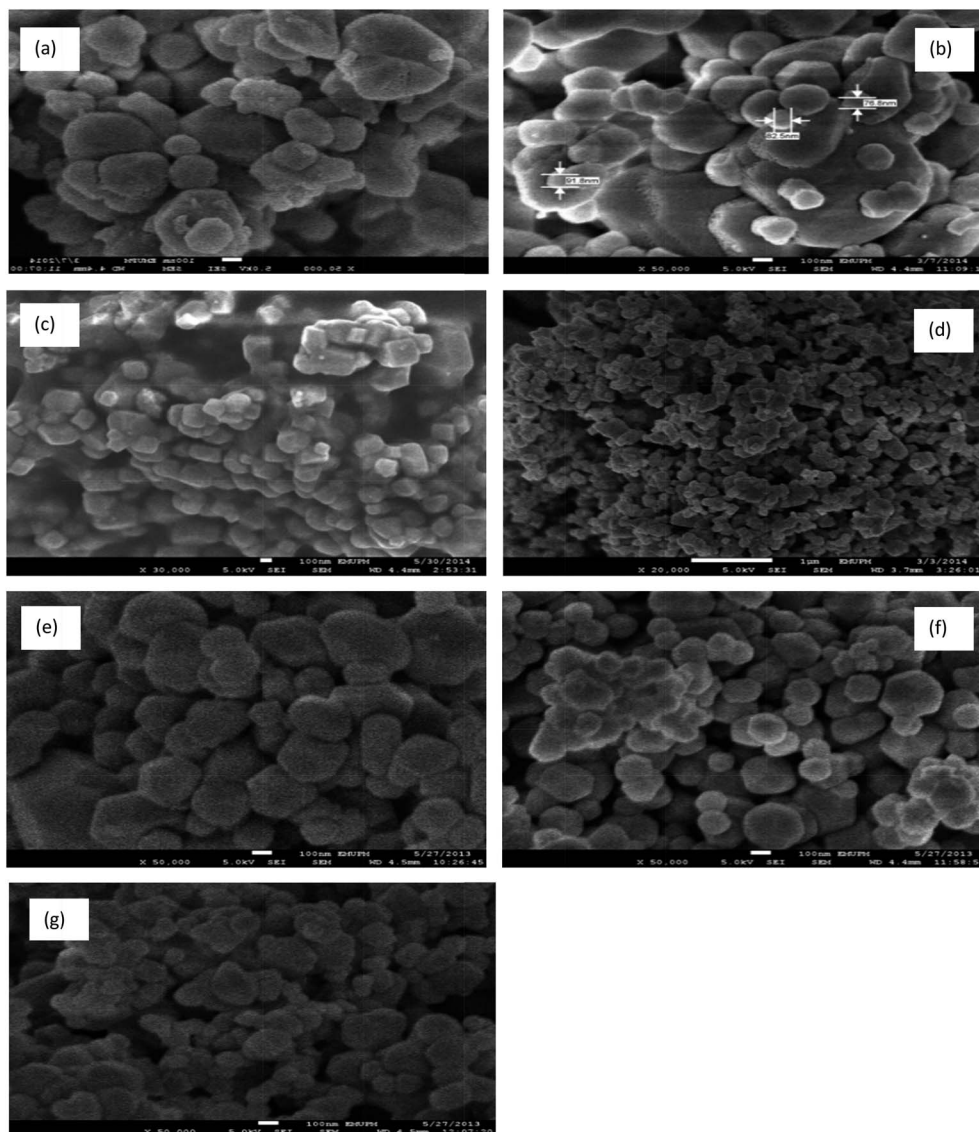
Fig. 5 FESEM images of catalysts: (a) Pd/MgO, (b) Pd/Mg$_{0.97}$Ce$_{0.03}$$^{3+}$O, (c) Pd/Mg$_{0.93}Ce_{0.07}$$^{3+}$O, (d) Pd/Mg$_{0.85}Ce_{0.15}$$^{3+}$O, (e) Pd/Mg$_{0.97}Ce_{0.03}$$^{4+}$O, (f) Pd/Mg$_{0.93}Ce_{0.07}$$^{4+}$O and (g) Pd/Mg$_{0.85}Ce_{0.15}$$^{4+}$O.

Pd/Mg$_{0.97}$Ce$_{0.03}$$^{3+}$O, which corresponds to the results obtained using the Scherrer equation.

3.1.5 Surface area and porosity of the catalyst. Table 2 presents the BET values of the specific surface areas (S_{BET}) and the pore properties of the reduced catalyst supports. The Pd/MgO catalyst had a pore radius of 11.4 Å, a pore volume of 0.2122 cm^3 g^{-1}, and a surface area of 15.7 m^2 g^{-1}. However, the addition of Ce$_2$O$_3$ as a promoter caused a reduction in both the surface area and volume. This decrease may be due to strong interactions between the palladium and magnesia–ceria support, and also due to pore blocking during the impregnation process. The observations of the present study agreed with earlier reports.[35] However, the addition of Ce$_2$O$_3$ prevented the loss of surface area during calcination at a temperature of 1150 °C, which resulted in an increase in the surface area of the catalyst (Table 2). Surface areas of 6.3, 7.5, and 16.6 m^2 g^{-1} were found for Pd/Mg$_{0.97}$Ce$_{0.03}$$^{3+}$, Pd/

Mg$_{0.93}$Ce$_{0.07}$$^{3+}$O and Pd/Mg$_{0.85}Ce_{0.15}$$^{3+}$O, respectively, while the surface areas of 8.1, 9.3, and 9.8 m^2 g^{-1} correspond to Pd/Mg$_{0.97}$Ce$_{0.03}$$^{4+}$, Pd/Mg$_{0.93}Ce_{0.07}$$^{4+}$O and Pd/Mg$_{0.85}Ce_{0.15}$$^{4+}$O.

It was observed that when the cerium size increased, the surface area also increased. The pore radii of all the catalysts were affected by the concentration of Ce$_2$O$_3$. The pore radii of Ce$_2$O$_3$ were 23.6, 24.3, and 90.1 Å for Pd/Mg$_{0.97}$Ce$_{0.03}$$^{3+}$O, Pd/Mg$_{0.93}Ce_{0.07}$$^{3+}$O and Pd/Mg$_{0.85}Ce_{0.015}$$^{3+}$O, respectively, whereas the pore radii of Ce$_2$O$_3$ were 23.3, 25.6, 3 and 0.9 Å for Pd/Mg$_{0.97}$Ce$_{0.03}$$^{4+}$O, Pd/Mg$_{0.93}Ce_{0.07}$$^{4+}$O and Pd/Mg$_{0.85}Ce_{0.015}$$^{4+}$O, respectively. After the addition of cerium, the pore volumes increased slightly, i.e. 0.0946, 0.1055, and 0.123 cm^3 g^{-1} for Pd/Mg$_{0.97}$Ce$_{0.03}$$^{3+}$O, Pd/Mg$_{0.93}Ce_{0.07}$$^{3+}$O and Pd/Mg$_{0.85}Ce_{0.015}$$^{3+}$O, respectively. These findings show that there is no apparent relation between the S_{BET} value and the pore volume of the catalysts.[36]

3.1.6 Temperature-programmed reduction (TPR). TPR-H_2 was used to characterize the reducibility of cerium for the reforming of Pd catalysts. Fig. 6a and Table 3 tabulate the profiles of TPR-H_2 for Pd/Mg$_{1-x}$Ce$_x^{3+}$O (where $x = 0.00$, 0.03, 0.07, and 0.15) and also illustrate the TPR-H_2 patterns of the catalysts. A peak appeared for the Pd/MgO catalyst when the temperature was 247 °C; this may be due to a reduction in the Pd–O crystallite.[37] Fig. 6a shows the TPR-H_2 profile for Pd/Mg$_{0.97}$Ce$_{0.03}^{3+}$O, Pd/Mg$_{0.93}$Ce$_{0.07}^{3+}$O, and Pd/Mg$_{0.85}$Ce$_{0.15}^{3+}$O as a cubic structure with three peaks. The first peak appeared when the temperatures of 215 °C, 213 °C and 232 °C were recorded for Pd/Mg$_{0.97}$Ce$_{0.03}^{3+}$O, Pd/Mg$_{0.93}$Ce$_{0.07}^{3+}$O, and Pd/Mg$_{0.85}$Ce$_{0.15}^{3+}$O, respectively, due to the reduction of Pd–O to Pd^0. The second peak appeared when temperatures of 494 °C, 503 °C and 508 °C were recorded for Pd/Mg$_{0.97}$Ce$_{0.03}^{3+}$O, Pd/Mg$_{0.93}$Ce$_{0.07}^{3+}$O, and Pd/Mg$_{0.85}$Ce$_{0.15}^{3+}$O, respectively. This observation corresponds to the reduction in the surface area of Ce$_2$O$_3$ in the Pd/Mg$_{1-x}$Ce$_x^{3+}$O catalysts. Moreover, a third peak appeared when temperatures of 749 °C, 754 °C and 764 °C were recorded for Pd/Mg$_{0.97}$Ce$_{0.03}^{3+}$O, Pd/Mg$_{0.93}$Ce$_{0.07}^{3+}$O, and Pd/Mg$_{0.85}$Ce$_{0.15}^{3+}$O, respectively, which is attributed to the bulk reduction of CeO$_2$. The second peak was reduced at lower temperatures due to the lower enthalpy of reduction, followed by a bulk reduction at higher temperatures. One possible reason for this could be the improved dispersion of Ce$_2$O$_3$ particles due to the incorporation of MgO into Ce$_2$O$_3$ and the retardation of sintering.[38] The other possible reason could be a stronger interaction between CeO$_2$ and Pd. The overlapping of the PdO peaks and the reduction of the CeO$_2$ peaks may have contributed to the strong interaction.[39] This resulted in the dispersion of a good promoter to the support and high interaction with the Pd species. It is deduced that the H_2-consumption of 224.6 μmol g^{-1} catalyst was used for the total reduction of PdO to Pd on Pd/MgO. The total amounts of H_2-consumption of the reduced Pd/Mg$_{0.97}$Ce$_{0.03}^{3+}$O, Pd/Mg$_{0.93}$Ce$_{0.07}^{3+}$O, and Pd/Mg$_{0.85}$Ce$_{0.15}^{3+}$O catalysts were calculated from the area of the three peaks. The findings of the catalysts were recorded as 312.5, 414.9, and 561.1 μmol g^{-1}, respectively. This may indicate the reduction of PdO and the partial reduction of Ce$_2$O$_3$. The addition of the Ce$_2$O$_3$ promoter increases the reducibility of the catalysts, especially for catalysts with MgO support. This may be due to the acid–base properties of the support. It is clear that Mg$_{1-x}$Ce$_x^{3+}$O, which has higher basicity than MgO, interacts strongly with the Ce$_2$O$_3$ promoter and results in greater PdO reduction with respect to the redox properties of Mg$_{1-x}$Ce$_x^{3+}$O.[36,40]

Moreover, Fig. 6b and Table 3 illustrate the TPR-H_2 profiles of Pd/Mg$_{0.97}$Ce$_{0.03}^{4+}$O, Pd/Mg$_{0.93}$Ce$_{0.07}^{4+}$O, and Pd/Mg$_{0.85}$Ce$_{0.15}^{4+}$O. The TPR-H_2 patterns of these catalysts were also similar to those of the previous catalysts. For all the three catalysts, it was detected that each catalyst had three distinct peaks. The temperatures recorded at the first peak were 210 °C, 217 °C and 233 °C, which were attributed to the reduction of Pd–O to Pd^0. The temperatures recorded at the second peak were 498 °C, 505 °C and 513 °C. This peak was attributed to the reduction of CeO$_2$ on the surface. Finally, the temperatures recorded at the final peak were 744 °C, 760 °C and 776 °C; this peak was attributed to the reduction of
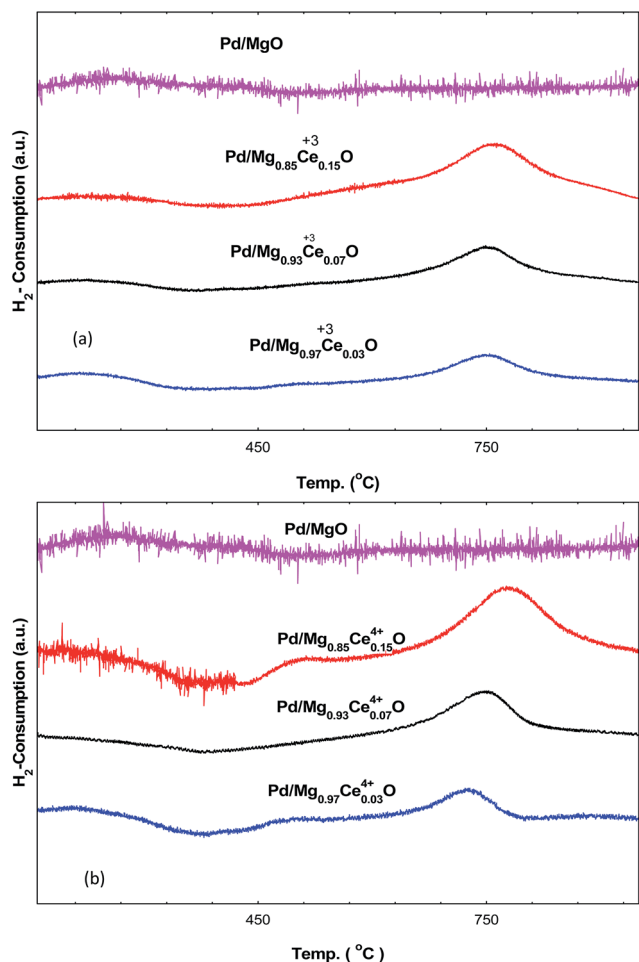

Fig. 6 TPR-H_2 profiles of catalysts (reduced in a 5% H_2/Ar stream at a temperature ramp of 10 °C min^{-1}) with (a) Ce^{3+} and (b) Ce^{4+} promoter.

Table 3 TPR-H_2 values of the catalysts

Catalyst	Temp. °C	Temp. °C	Temp. °C	Amount H_2-gas adsorbed μmol g^{-1}
Pd/MgO	247	—	—	224.6
Pd/Mg$_{0.97}$Ce$_{0.03}^{3+}$O	215	494	749	312.5
Pd/Mg$_{0.93}$Ce$_{0.07}^{3+}$O	213	503	754	414.9
Pd/Mg$_{0.85}$Ce$_{0.15}^{3+}$O	232	508	764	561.1
Pd/Mg$_{0.97}$Ce$_{0.03}^{4+}$O	210	498	744	267.8
Pd/Mg$_{0.93}$Ce$_{0.07}^{4+}$O	217	505	760	388.9
Pd/Mg$_{0.85}$Ce$_{0.15}^{4+}$O	233	513	776	456.5
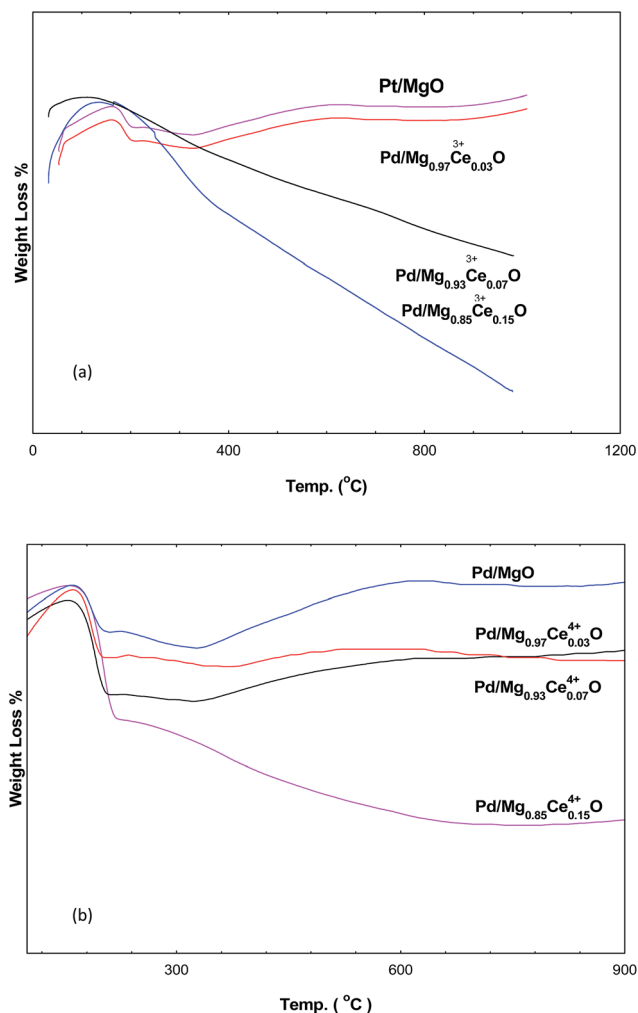
Fig. 7 TG of the catalysts with (a) Ce^{3+} and (b) Ce^{4+} promoter.

estimated weight losses for Pd/MgO, Pd/$Mg_{0.97}Ce_{0.03}^{3+}$O, Pd/$Mg_{0.93}Ce_{0.07}^{3+}$O, and Pd/$Mg_{0.85}Ce_{0.15}^{3+}$O catalysts were recorded to be 1.5%, 2.2%, 1.8% and 1.6%, respectively. In addition, the estimated weight losses for Pd/$Mg_{0.97}Ce_{0.03}^{4+}$O, Pd/$Mg_{0.93}Ce_{0.07}^{4+}$O, and Pd/$Mg_{0.85}Ce_{0.15}^{4+}$O catalysts were recorded to be 2.0%, 1.7% and 1.6%, respectively. The graphs presented below as Fig. 7 show the entire weight loss profile of the compound. There was a slight initial increase due to the adsorption of the N_2 gas on the compound. All the compounds became thermally stable at 500 °C, which corresponds to the high melting points of magnesia and ceria at 2852 °C and 2177 °C, respectively. This also helps in establishing good interaction among the components of the catalyst. Fig. 7b illustrates the components of the other catalysts: Pd/$Mg_{0.97}Ce_{0.03}^{4+}$O, Pd/$Mg_{0.93}Ce_{0.07}^{4+}$O, and Pd/$Mg_{0.85}Ce_{0.15}^{4+}$O. The findings of the thermal analysis were similar and consistent with the results of Mojovic et al.[42]

3.2. Catalytic performance in biogas reforming

3.2.1 Effect of reactant concentration on conversion. The conversion of CH_4 and CO_2 and the selectivity, which is defined
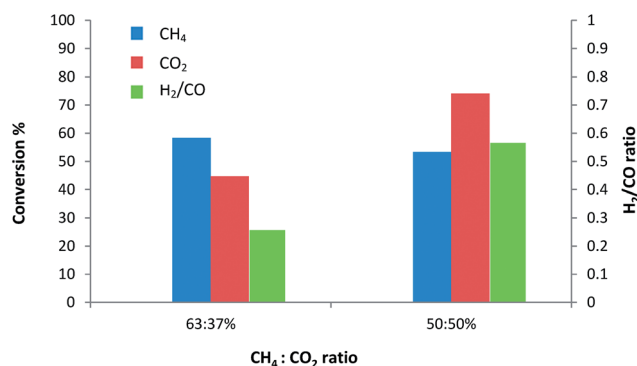

Fig. 8 The effects of changing the concentration ratio of CH_4 : CO_2 (reactant 1 – 2 : 1; reactant 2 – 1 : 1) on % conversion and H_2/CO ratio for the Pd/$Mg_{0.85}Ce_{0.15}^{3+}$O catalyst at 900 °C.
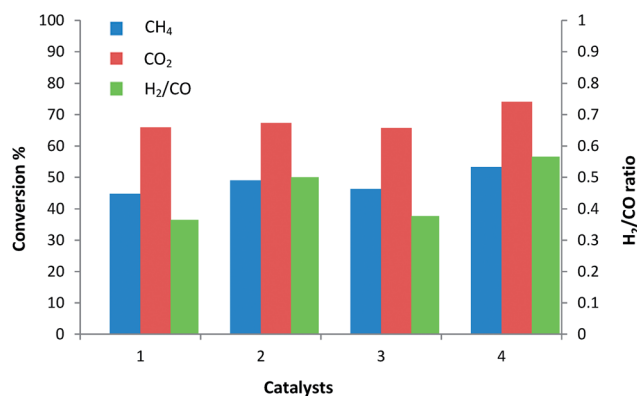

Fig. 9 The effects of using different catalysts: (1) Pd/MgO, (2) Pd/$Mg_{0.97}Ce_{0.03}^{3+}$O, (3) Pd/$Mg_{0.93}Ce_{0.07}^{3+}$O, and (4) Pd/$Mg_{0.85}Ce_{0.15}^{3+}$O on CH_4, CO_2 conversion and H_2/CO ratio at 900 °C for the 1 : 1 ratio of CH_4 : CO_2.

bulk CeO_2 for Pd/$Mg_{0.97}Ce_{0.03}^{4+}$O, Pd/$Mg_{0.93}Ce_{0.07}^{4+}$O, and Pd/$Mg_{0.85}Ce_{0.15}^{4+}$O, respectively. The best explanation for the high decrease in temperature of Pd/$Mg_{1-x}Ce_x^{4+}$O as compared to that of Pd/$Mg_{1-x}Ce_x^{3+}$O may be the emergence of overlapping peaks after the reduction of PdO and CeO_2.[41] As the Ce^{3+} ion is less charged and bigger in size than the Ce^{4+} ion, Ce^{3+} is more easily reduced. Based on the area of the two peaks, the H_2 consumptions of Pd/$Mg_{0.97}Ce_{0.03}^{4+}$O, Pd/$Mg_{0.93}Ce_{0.07}^{4+}$O, and Pd/$Mg_{0.85}Ce_{0.15}^{4+}$O reduction were recorded as 267.8, 388.9 and 456.5 μmol g^{-1} catalyst, respectively. The TPR-H_2 results reveal that the Pd/$Mg_{0.85}Ce_{0.15}^{3+}$O catalyst showed the highest number of active sites among the catalysts. Thus, it can be concluded that Pd/$Mg_{0.85}Ce_{0.15}^{3+}$O was the best catalyst in the present study.

3.1.7 Thermal analysis study. Fig. 7a shows the TGA analysis for the reduced catalysts: Pd/MgO, Pd/$Mg_{0.97}Ce_{0.03}^{3+}$O, Pd/$Mg_{0.93}Ce_{0.07}^{3+}$O, and Pd/$Mg_{0.85}Ce_{0.15}^{3+}$O. The results revealed that there was a weight loss at only one stage for all the catalysts. The estimated weight loss, which was approximately 2%, occurred in the temperature range between 100 °C and 150 °C. This can be attributed to the removal of moisture from the Pd/$Mg_{1-x}Ce_x$O catalysts, as shown in Fig. 7a. In contrast, the

Table 4 The catalytic results of DRM reaction for the catalysts at 900 °C for the 1 : 1 ratio of $CH_4 : CO_2$

Sample name	CH_4 conversion%	CO_2 conversion%	H_2/CO ratio
Pd/MgO	45	66	0.3
Pd/Mg$_{0.97}$Ce$_{0.03}$$^{3+}$O	49	67	0.5
Pd/Mg$_{0.93}$Ce$_{0.07}$$^{3+}$O	46	66	0.4
Pd/Mg$_{0.85}$Ce$_{0.15}$$^{3+}$O	54	74	0.6
Pd/Mg$_{0.97}$Ce$_{0.03}$$^{4+}$O	38	53	0.2
Pd/Mg$_{0.93}$Ce$_{0.07}$$^{4+}$O	45	58	0.5
Pd/Mg$_{0.85}$Ce$_{0.15}$$^{4+}$O	34	54	0.2

in terms of the H_2/CO ratio, indicated that dry reforming reaction activity occurred. When the temperature increased above 900 °C, blank tests (reaction without catalyst) showed the existence of H_2 and CO in the outlet gas. This may be due to the methane decomposition reaction (eqn (4)). When Mg$_{1-x}$Ce$_x$O was used without Pd, the CH_4 and CO_2 conversions were recorded as low readings of 38% and 48%, respectively, whereas the H_2/CO ratio was recorded as 0.2%. These results indicated that there may be a weak reaction on the promoter pores of the support, which were presented in the BET results. On the other hand, when the Pd/Mg$_{1-x}$Ce$_x$$^{3+}$O catalysts were used, the rates of conversion of CH_4 and CO_2 and the H_2/CO ratio increased. Fig. 8 illustrates the effects of the reactant ratio on the H_2/CO ratio and CO_2 conversion. The concentration of CO_2 ($CH_4 : CO_2$, 1 : 1) increased, followed by an increase in the conversion of CO_2 as well as an increase in H_2/CO ratio. This occurrence could be due to the decrease in the carbon deposition on the surface of the catalyst that reacted with excess CO_2 to produce CO (eqn (6)). In other words, the Pd metal doped on the support plays a crucial role in the catalytic reaction. It was observed that the Pd/Mg$_{0.85}$Ce$_{0.15}$O catalyst recorded conversions of 54% and 74% for $CH_4 : CO_2$ (1 : 1) and a H_2/CO ratio of 0.6. However, the conversions of CH_4 and CO_2 gases were recorded to be 58% and 45%, respectively; the ratio was 2 : 1 and the H_2/CO ratio was 0.3. This finding indicated that the greatest resistance to the deactivation of the catalyst occurred at the ratio of 1 : 1 due to carbon formation, which increased the selectivity of H_2 and CO (Fig. 8). The same results were also obtained from the other reported catalysts.[43]

3.2.2 Effect of catalyst concentration on conversion. Fig. 9 and Table 4 illustrate the effects of the concentration of the catalysts on the conversion process. It can be seen that the values of CH_4 and CO_2 conversion and the H_2/CO ratio were 45%, 66% and 0.3 for the Pd/MgO catalyst, whereas the Pd/Mg$_{0.97}$Ce$_{0.03}$$^{3+}$O catalyst showed 49%, 67% and 0.5, and for the Pd/Mg$_{0.93}$Ce$_{0.07}$$^{3+}$O catalyst, the values were 46%, 66% and 0.4, respectively. The highest values were reported for Pd/Mg$_{0.85}$Ce$_{0.15}$$^{3+}$O catalyst as 54%, 74% and 0.6 for the CH_4 and CO_2 conversion and H_2/CO ratio, respectively.

In this study, the favorable results may be due to strong interactions between the Pd metal and the support as well as the strong basicity of the support. In previous studies, Laosiripojana[44] and Guo et al.[45] showed unfavorable results. This was because the researchers used the Ni/Al$_2$O$_3$ catalyst, which had

weak interactions between Ni and the support Al$_2$O$_3$; moreover, the catalyst produced alumina with low basicity.

The increasing order of CH_4 and CO_2 conversion and the H_2/CO ratio can be presented as follows: Pd/MgO < Pd/Mg$_{0.97}$Ce$_{0.03}$$^{3+}$O < Pd/Mg$_{0.93}Ce_{0.07}$$^{3+}$O < Pd/Mg$_{0.85}Ce_{0.15}$$^{3+}$O. This means that the most effective catalyst was Pd/Mg$_{0.85}$Ce$_{0.15}$O. The results indicated that the rate of the formation of CO in the dry reforming of methane depends on the amount of Ce$_2$O$_3$–MgO solid solution in the catalyst.[46] It may be concluded that the greater the amount of solid solution, the higher is the rate of formation of CO. Thus, the formation of a solid solution plays an important role in the generation of active sites for the CO_2 reformation of methane. This occurs because all the Ce$_2$O$_3$ is like a solid solution, which stabilizes both oxides. Only the surface Ce$_2$O$_3$ layer of the catalyst in the Ce$_2$O$_3$–MgO solid solution was reduced at 700 °C. The Ce sites that were generated remained in close contact with the solid solution, which hindered the Ce sintering.[46] In addition, the activity of the Pd/Mg$_{0.85}$Ce$_{0.15}$$^{3+}$O catalyst was greater than the activity of the Pd/Mg$_{0.85}$Ce$_{0.15}$$^{4+}$O catalyst. This may be because the charge of Ce^{3+} is lower than the charge of Ce^{4+}. In this way, reduction occurs more readily, while Ce is produced on the surface of the catalyst.

Furthermore, Pd particles can be found in the sites responsible for the catalytic process because the Pd particles have strong interactions with MgO–Ce$_2$O$_3$. It is also noted that increasing the Pd concentration in the support did not change the CH_4 conversion and CO_2 conversion and selectivity. This can be attributed to the formation of strong Lewis basicity with a metal oxide support. The increase in the Lewis basicity of the support subsequently increased the ability of the catalyst in the dry reforming of methane for the chemisorption of CO_2. Besides, the adsorbed CO_2 will react with C to form CO (eqn (6)), which leads to a reduction in coke formation. The formation of the Ce$_2$O$_3$–MgO solid solution also provides a specific approach to suppress the deposition of carbon. MgO is linked to a strong Lewis base, with a high amount of CO_2 on the surface of the catalyst, which can decrease or prevent carbon formation. Furthermore, the XPS results showed that the reduction of Ce$_2$O$_3$ was much more difficult with the Ce$_2$O$_3$–MgO solid solution than with the solid solution of pure Ce$_2$O$_3$. The
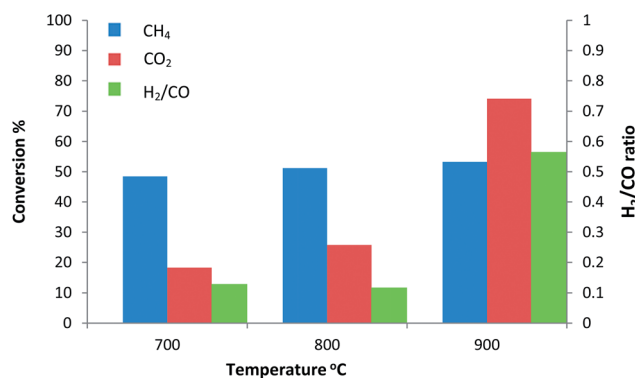

Fig. 10 The influence of temperature on the catalytic activity of the Pd/Mg$_{0.85}$Ce$_{0.15}$$^{3+}$O catalyst. (1) 700 °C, (2) 800 °C and (3) 900 °C for the 1 : 1 ratio of $CH_4 : CO_2$.

reduction may lead to the formation of small particles of cerium on the surface.[47,48] The combination of the surface basicity and the small metal particle size (Table 2) affects the carbon deposition by the MgO-based solid solution catalysts.

Furthermore, the high conversion rate of CH_4 and CO_2 was due to the particle size involved in the reaction activity. The doping metal Pd was prepared based on the Debye–Scherrer equation and supported by TEM analysis. Its particle size was on the nano scale. Thus, it is evident that particle size plays a significant role in the reaction activity. Any increase in the conversion of reactants and the selectivity (yield) can be attributed to the reduction of particles into nano-ranged sizes, which can lead to an increase of 16.6 m^2 g^{-1} in the surface area and 561.1 μmol g^{-1} of active sites (Table 2).

3.2.3 Effects of temperature on conversion. Fig. 10 shows the activity and selectivity results of the $Pd/Mg_{0.85}Ce_{0.15}O$ catalyst in the temperature range from 700 to 900 °C. In general, the conversion of $CH_4 : CO_2$ (1 : 1) showed an increase when the temperature was increased from 700 °C to 900 °C. This may be due to the strong endothermicity of the dry-reforming reaction (eqn (2)). Earlier studies had shown that higher temperatures increased the rate of conversion.[49] It is noted that when there was an increase in temperature from 700 °C to 900 °C, the CH_4 conversion of $Pd/Mg_{0.85}Ce_{0.15}O$ showed an increase from 48% to 54%, and the CO_2 conversion also increased from 18% to 74%. However, when the temperature was above 900 °C, there was no evident increase in the conversion rates of CH_4 and CO_2. Fig. 10 shows the H_2/CO ratio of the catalyst at different temperatures. When the temperature was below 900 °C, the H_2/CO ratio of the samples was recorded at <1. The reverse water-gas-shift reaction (RWGS) (eqn (2)) might consume extra H_2 and produce CO, which causes a decrease in the H_2/CO ratio. When the temperature was at 900 °C, the H_2/CO ratio of $Pd/Mg_{0.85}Ce_{0.15}O$ was recorded to be 0.6, which indicates a small contribution from the RWGS reaction (eqn (3)).[50] Table 3 shows that the activity and selectivity of $Pd/Mg_{1-x}Ce_x{}^{3+}O$ was higher than that of $Pd/Mg_{1-x}Ce_x{}^{4+}O$ in DRM. This might be because Ce(III)-based catalysts are superior to Ce(IV)-based catalysts because of the lower charge and greater size of the Ce^{3+} ion, as well as its more ready reduction to Ce.[51]
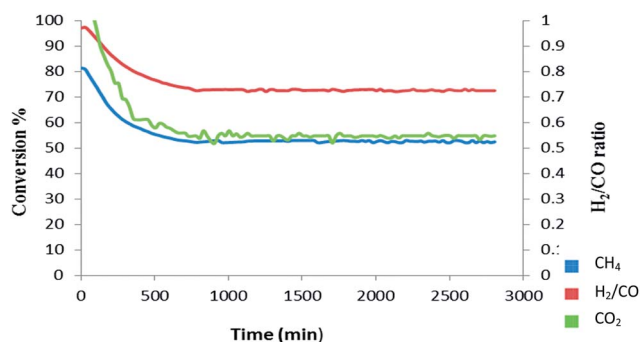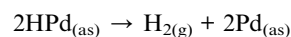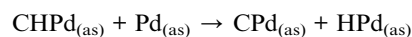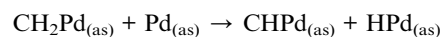
3.2.4 Stability tests. Fig. 11 shows the findings of the temperature tests. It is observed that at 900 °C, the conversions for both CH_4 and CO_2 were high. In general, CH_4 is only adsorbed on the palladium metal and dissociates to yield hydrogen and hydrocarbon species CH_x ($x = 0–4$), if $x = 0$. The deposition of carbon on the surface of Pd metal[52] is elaborated through the following mechanisms:

$$CH_4 + 2Pd_{(as)} \rightarrow CH_3Pd_{(as)} + HPd_{(as)}$$

$$CH_3Pd_{(as)} + Pd_{(as)} \rightarrow CH_2Pd_{(as)} + HPd_{(as)}$$

$$CH_2Pd_{(as)} + Pd_{(as)} \rightarrow CHPd_{(as)} + HPd_{(as)}$$

$$CHPd_{(as)} + Pd_{(as)} \rightarrow CPd_{(as)} + HPd_{(as)}$$

$$2HPd_{(as)} \rightarrow H_{2(g)} + 2Pd_{(as)}$$
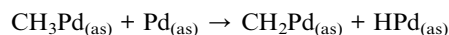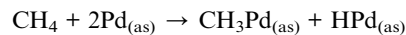
Nakamura et al.[53] investigated the effects of the catalyst promoter on the dry reformation of methane. According to the mechanisms, CO_2 was activated in proximity to the metal particle on the support to form a carbonate species. Finally, carbonate was reduced by CH_x species to form carbon monoxide (CO).

$$CO_{2(g)} \rightarrow CO_{2(support)}$$

$$CO_{2(support)} + O^{2-}{}_{(support)} \rightarrow CO_3{}^{2-}{}_{(support)}$$

$$2H_{(metal)} \rightarrow 2H_{(support)}$$

$$CO_3{}^{2-}{}_{(support)} + 2H_{(support)} \rightarrow HCO_2{}^{1-}{}_{(support)} + OH^{1-}{}_{(support)}$$

$$CO_{(support)} \rightarrow CO_{(g)}$$

The function of the Ce_2O_3 promoter in the catalyst is to produce high stability and provide resistance against coking. This was confirmed by the results obtained from the conversion of CO_2 and CH_4 as well as the H_2/CO ratio for over 50 h of reaction. The formation of carbon on the palladium surface of
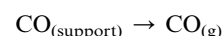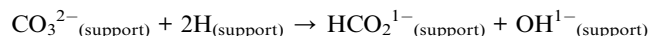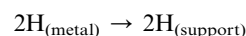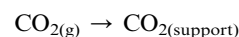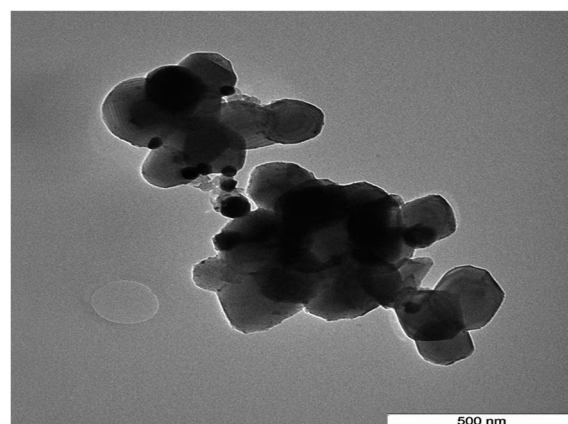

Fig. 11 Stability tests of $Pd/Mg_{0.85}Ce_{0.15}{}^{3+}O$ catalysts at 900 °C for the 1 : 1 ratio of $CH_4 : CO_2$ for 50 h (GHSV = 15 000 ml g cat^{-1} h^{-1}, atmospheric pressure).

Fig. 12 TEM analysis of spent $Pd/Mg_{0.85}Ce_{0.15}{}^{3+}O$ catalyst after reaction at 900 °C and CH_4/CO_2 ratio of 1 : 1.
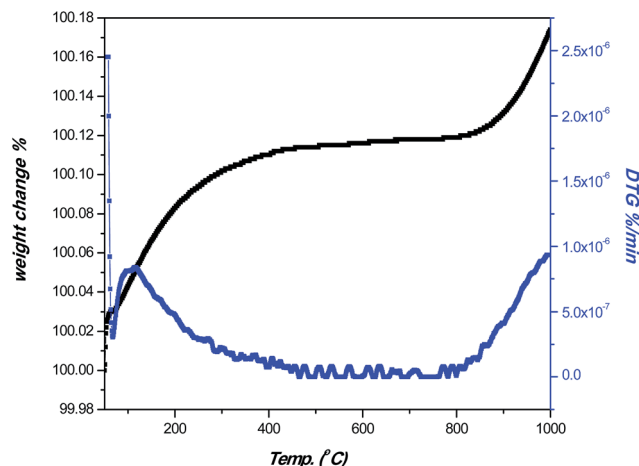
Fig. 13 TGA and DTG profiles of spent $Pd/Mg_{0.85}Ce_{0.15}^{3+}O$ catalyst (20 ml min^{-1} O_2 stream under a temperature ramp of 10 °C min^{-1}).

the catalyst in the dry reforming of methane was eliminated by Ce_2O_3. While the CO_2 adsorption was enhanced by increasing the basicity of Ce_2O_3; the formation of carbonate species occurs mainly on Ce_2O_3; the carbonate dissociates into CO_2, which then dissociates into CO and O. The oxygen then reacts with the carbon deposited on the Pd metal to produce CO.[54] When the concentrations of Ce_2O_3 were low, the CO_2 conversion increased through the formation of strong ionic oxide $Ce_2O_2CO_3$, which resulted in the adsorption of CO_2 on the surface of the catalyst. This reaction increased the conversion of CH_4. When Ce_2O_3 was found in higher concentrations, the conversion of both CH_4 and CO_2 attenuated. This is most likely due to the increase in the electron density of Pd.[55] The $Ce_2O_2CO_3$ species participates directly in DRM, where it decomposes to produce CO; this provides oxygen species to react with the carbon deposits at the interface of $Pd–Ce_2O_2CO_3$. Following this activity, the Pd sites were restored. Likewise, Ce_2O_3 enabled the catalysts to dissociate in the adsorbed CO_2.

$$CO_{2(g)} \rightarrow CO_{(support)} + O_{(promoter)}$$

$$C_{(metal)} + O_{(promoter)} \rightarrow CO_{2(g)}$$

Fig. 13 illustrates the thermograms in two different temperature regions. At the first stage of the temperature range, there was a decrease in the weight of the spent catalyst. On the contrary, there was an increase in the weight at a higher temperature. When the temperature was at 650 °C, the weight loss was attributed to the oxidation of the carbon deposit. The carbon deposited on the spent catalyst was considered to be carbon layered. Further layering of carbon was found in the absence of filamentous carbon, as indicated in the TEM results of the spent catalysts (refer to Fig. 12). The amount of coke deposited on the spent catalysts was calculated to be 1% wt. In conclusion, these results showed that a small amount of coke was deposited on the catalysts, and the formation of coke was likely due to dispersion of the metal catalysts. The smaller

crystal size of the metal catalysts makes them less prone to deactivation. This finding was in line with the reported results by Zhu *et al.*[56]

4. Conclusions

A co-precipitation method was used to prepare samples of $Pd/Mg_{1-x}Ce_x^{3+}O$ and $Pd/Mg_{1-x}Ce_x^{4+}O$ (x = 0.00, 0.03, 0.07, and 0.15) (with 1% wt Pd loading) with K_2CO_3 as a precipitant. These samples were used as catalysts for the syngas synthesis after the reaction of CO_2, reforming methane under ideal reaction conditions at T = 900 °C and CH_4/CO_2 = 1/1 with the $Pd/Mg_{0.85}Ce_{0.15}^{3+}O$ catalyst. The results of the XRD analysis showed that traces of Ce_2O_3 were found in the MgO lattices and also on the surfaces of the catalysts. The findings also revealed that some photoelectron signals were emitted from C1s, Mg2p, O1s, Pd3d, and Ce3d. The TPR results showed that the reducibility of Ce_2O_3 was increased by an increase in Ce_2O_3 in the support with high active sites on the surface of the catalyst. For the dry reforming of methane, CO_2 and CH_4 conversions of 74% and 54%, respectively, were recorded for the $Pd/Mg_{1-x}Ce_x^{3+}O$ catalyst. This result was higher than that for the $Pd/Mg_{1-x}Ce_x^{4+}O$ catalyst at 900 °C. In addition, the CO_2 and CH_4 conversions for the $Pd/Mg_{1-x}Ce_x^{4+}O$ catalyst were found to be lower than that for the $Pd/Mg_{1-x}Ce_x^{3+}O$ catalyst due to the smaller size of Ce^{4+} ion. Finally, the more positively charged Ce^{4+} ion is less readily reduced than the Ce^{3+} ion in the catalyst.

Acknowledgements

Notes and references

1 D. C. Carvalho, H. S. Souza, M. Josué Filho, E. M. Assaf, V. V. Thyssen, A. Campos and A. C. Oliveira, *RSC Adv.*, 2014, **4**, 61771–61780.
2 A. R. McFarlane, I. P. Silverwood, R. Warringham, E. L. Norris, R. M. Ormerod, C. D. Frost and D. Lennon, *RSC Adv.*, 2013, **3**, 16577–16589.
3 R. G. Gonzalez, *Petrol. Tech. Q.*, 2006, **11**, 61–62.
4 J. G. Zhang, H. Wang and K. D. Ajay, *J. Catal.*, 2007, **249**, 300–310.
5 Z. L. Zhang and X. E. Verykios, *Catal. Today*, 1994, **21**, 589–595.
6 E. Ruckenstein and Y. H. Hu, *Adv. Catal.*, 2004, **48**, 297–345.
7 H. B. Nussler and O. Kubaschewski, *Z. Phys. Chem.*, 1980, **121**, 187–195.
8 V. M. Shinde and G. Madras, *RSC Adv.*, 2014, **4**, 4817–4826.
9 J. T. Richardson, M. Garrait and J. K. Hung, *Appl. Catal., A*, 2003, **255**, 69–82.
10 K. Seshan, H. W. Ten Barge, W. Halty, A. N. J. van Keulen and J. R. H. Ross, *Stud. Surf. Sci. Catal.*, 1994, **81**, 285–290.

11 K. Tao, S. Zhou, Q. Zhang, C. Kong, Q. Ma, N. Tsubaki and L. Chen, *RSC Adv.*, 2013, **3**, 22285–22294.

12 J. A. C. Dias and J. M. Assaf, *Catal. Today*, 2003, **85**, 59–68.

13 J. Juan-Juan, M. C. Romn-Martnez and M. J. Illn-Gmez, *Appl. Catal., A*, 2006, **301**, 9–15.

14 A. E. C. Luna and M. E. Iriarte, *Appl. Catal., A*, 2008, **343**, 10–15.

15 K. C. Mondal, V. R. Choudhary and U. A. Joshi, *Appl. Catal., A*, 2007, **316**, 47–52.

16 D. Dong, X. Shao, Z. Wang, C. Lievens, J. Yao, H. Wang and C. Z. Li, *RSC Adv.*, 2013, **3**, 1341–1345.

17 Q. Zhang, T. Wu, P. Zhang, R. Qi, R. Huang, X. Song and L. Gao, *RSC Adv.*, 2014, **4**, 51184–51193.

18 H. Kambolis, A. Matralis, C. Trovarelli and C. H. Papadopoulou, *Appl. Catal., A*, 2010, **377**, 16–26.

19 J. L. G. Fierro, J. Soria, J. Sanz and J. M. Rojo, *J. Solid State Chem.*, 1987, **66**, 154–162.

20 A. Trovarelli, *Catal. Rev.: Sci. Eng.*, 1996, **38**, 439–520.

21 S. Damyanova, B. Pawelec, K. Arishtirova, M. V. Martinez-Huerta and J. L. G. Fierro, *Appl. Catal., B*, 2009, **89**, 149–159.

22 J. Chen, Q. Wu, J. Zhang and J. Zhang, *Fuel*, 2008, **87**, 2901–2907.

23 K. Tomishige, *Catal. Today*, 2004, **89**, 405–418.

24 F. W. Aldbea, N. Ibrahim, M. H. Abdullah and R. E. Shaiboub, *J. Sol-Gel Sci. Technol.*, 2012, **62**, 483–489.

25 P. Grange, *Catal. Rev.: Sci. Eng.*, 1980, **21**, 135–181.

26 X. Wang, L. Meng, F. Wu, L. Wang and X. Mu, *Green Chem.*, 2012, **14**, 758–767.

27 S. A. Sadeek, *J. Argent. Chem. Soc.*, 2005, **93**, 165–175.

28 K. Walter, O. Seiferth, J. Libuda, H. Kuhlenbeck, M. Bäumer and H.-J. Freund, *Surf. Sci.*, 1998, **402**, 428–432.

29 F. Skoda, M. P. Astier, G. M. Pajonk and M. Primet, *Catal. Lett.*, 1994, **29**, 159–168.

30 M. Zhiijian, L. Ying, F. Maohong, Z. Ling and Z. Ji, *J. Chem. Eng.*, 2015, **259**, 293–302.

31 C. Hidalgo, S. Jalila, M. Alberto, M. Jose and S. Said, *J. Colloid Interface Sci.*, 2012, **382**, 67–73.

32 E. Ruckenstein and Y. H. Hu, *Chem. Innovation*, 2000, **30**, 39–43.

33 X. Chen, J. Jiang, F. Yan, S. Tian and K. Li, *RSC Adv.*, 2014, **4**, 8703–8710.

34 L. Qian, Z. Ma, Y. Ren, H. Shi, B. Yue, S. Feng, J. Shen and S. Xie, *Fuel*, 2014, **122**, 47–61.

35 B. Saha, A. Khan, H. Ibrahim and R. Idem, *Fuel*, 2014, **120**, 202–217.

36 Y. H. Taufiq-Yap, Sudarno, U. Rashid and Z. Zainal, *Appl. Catal., A*, 2013, **468**, 359–369.

37 G. Li, L. Hu and M. Hill, *Appl. Catal., A*, 2006, **301**, 16–24.

38 M. Fernandez-Garcia, A. Martiner-Arias and A. IglesiasJuez, *J. Catal.*, 2000, **194**, 385–392.

39 Y. W. Chao and P. K. Shen, *Int. J. Hydrogen Energy*, 2012, **37**, 4107–4118.

40 S. Tada, T. Shimizu, H. Kameyama and T. Haneda, *Int. J. Hydrogen Energy*, 2012, **37**, 5527–5531.

41 V. M. Gonzalez-Delacruz, F. Ternero, R. Peren, A. Caballero and J. P. Holgado, *Appl. Catal., A*, 2010, **384**, 1–9.

42 Z. Mojovic, S. Mentus and Z. Tesic, *Mater. Sci. Forum*, 2004, **453**, 257–263.

43 A. M. Gadalla and M. E. Sommer, *Chem. Eng. Sci.*, 1989, **44**, 2825–2829.

44 N. Laosiripojana and S. Assabumrungrat, *Appl. Catal., B*, 2005, **60**, 107–116.

45 J. Guo, H. Lou, H. Zhao, D. Chai and X. Zheng, *Appl. Catal., A*, 2004, **273**, 75–82.

46 A. Zecchina, G. Spoto and S. Coluccia, *J. Chem. Soc., Faraday Trans. 1*, 1984, **80**, 1891–1901.

47 Y. H. Hu and E. Ruckenstein, *Catal. Rev.*, 2002, **44**, 423–453.

48 K. Tomishige, Y. Himeno, Y. Matsuo, Y. Yoshinaga and K. Fujimoto, *Ind. Eng. Chem. Res.*, 2000, **39**, 1891–2021.

49 S. Appari, V. M. Janardhanan, R. Bauri, S. Jayanti and O. Deutschmann, *Appl. Catal., A*, 2014, **471**, 118–125.

50 J. Kehres and Jakobsen, *J. Phys. Chem. C*, 2012, **116**, 12407–21415.

51 D. L. Trimm, *Catal. Today*, 1997, **37**, 233–238.

52 A. Topalidis, D. E. Petrakis, A. Ladavos, L. Loakatzikou and P. J. Pomonis, *Catal. Today*, 2007, **127**, 238–245.

53 J. Nakamura, K. Aikawa, K. Sato and T. Uchijima, *Catal. Lett.*, 1994, **25**, 265–270.

54 T. Osaki and T. Mori, *J. Catal.*, 2001, **204**, 89–97.

55 J. A. C. Dias and J. M. Assaf, *Catal. Today*, 2003, **85**, 59–68.

56 J. Zhu, X. Peng, L. Yao, J. Shen, D. Tong and C. Hu, *Int. J. Hydrogen Energy*, 2011, **36**, 7094–7104.